Generative Displacement Model

A Preprint

A. Sakhaee-Pour *
Department of Petroleum Engineering
Department of Electrical and Computer Engineering
University of Houston
Houston, Texas 77204, USA

Abstract

Generative models are often based on statistical physics or game theory, such as Latent Diffusion Models (LDMs) or Generative Adversarial Networks (GANs). This study relies on two-phase displacement in porous media, where one fluid displaces another, to introduce a Generative Displacement Model (GDM). The introduced model uses weight functions derived from effective density and flow rate in the latent space. The weight functions are compared with the mixing rules of diffusion-based models, providing insight into generative behavior and performance. The proposed approach is evaluated using 5,508 shale fracture images and benchmarked against an LDM. A grid search was conducted using 200,000 training steps over learning rates from 1×10^{-5} to 5×10^{-5}. The best-performing GDM achieved a Fréchet Inception Distance (FID) of 15.7, comparable to 16.6 for the LDM trained similarly, though hyperparameters beyond learning rate were not tuned. The generated images show realistic fracture patterns and surface textures of the original dataset. The results show that multiphase transport physics offers an interesting and less explored basis for generative model design.

Keywords Generative AI; multiphase transport; porous media; latent space

1 Introduction

Researchers use generative artificial intelligence to model complex physical systems, especially where data are sparse or costly to obtain (Nguyen et al. 2022). Relevant applications include drug delivery (Sahimi 2025) and biological porous media (Sahimi and Sahimi 2025). Goodfellow et al. (2016) discussed the foundation of generative models using deep learning. Later, Chollet (2021) described how these methods scale to complex, high-dimensional data.

Many subsurface processes depend on multiphase fluid transport in porous media. Walsh and Lake (2003) and Lake et al. (2014) describe the underlying physics and equations. The underlying physics control carbon dioxide storage (Benson and Cole 2008), shale-gas recovery (Sakhaee-Pour and Bryant 2012), and underground hydrogen storage (Zivar et al. 2021). Nevertheless, data required to build subsurface models are limited due to limited accessibility. Generative models are an effective tool to address this limitation. For instance, Ferreira et al. (2022) developed a style-based GAN to create realistic images, addressing the scarcity of geoscience data.

Researchers have used generative models to reconstruct pore structures from limited data. Zhang et al. (2023) reconstructed shale void space using a GAN. Amiri et al. (2023) employed a GAN to characterize the microstructure of earth materials from higher-order spatial correlations. Zhu et al. (2024) used an improved Wasserstein GAN to create pore-space images with realistic morphology. Lyu and Ren (2024) applied a diffusion-based generative model to reconstruct random porous microstructures. Ugolkov et al. (2025) used a GAN to enhance the resolution of segmented rock tomography. Generative models have also supported reservoir simulation, as Fan et al. (2024) employed them to build multiple realizations. Ranazzi et al. (2024) reported that generative models enhanced simulation stability. de Castro Vargas Fernandes et al. (2024) used a GAN to estimate rock permeability from microtomography images, addressing the high cost of acquiring high-resolution data.

*Corresponding author: asakhaee@central.uh.edu

Another relevant challenge is fracture characterization. Researchers have developed innovative methods for fracture characterization using small samples (Alipour et al. 2021), but their applicability is still limited by the scarcity of subsurface samples. Generative models offer a potential solution through data augmentation. Salimzadeh et al. (2023) used generative models to characterize fractures. They reported that the models learned the underlying patterns and geomechanical properties, while also highlighting the computational efficiency of the generative approach.

Two types of generative models have become increasingly popular. The first is GAN based on the competition between two networks that reach a Nash equilibrium (Goodfellow et al. 2014). Diffusion-based models represent a second major category (Sohl-Dickstein et al. 2015; Ho et al. 2020; Song et al. 2020; Rombach et al. 2022), derived from non-equilibrium molecular diffusion in statistical physics. Although both approaches have been used extensively, the limited scope of their underlying inspirations suggests that other generative models may exist. Exploring such a model is valuable given the rapid evolution and diversification of generative AI.

This paper proposes a Generative Displacement Model (GDM) to create realistic complex fractures in shale. The model mimics multiphase displacement in porous media by implementing the constitutive equations of density and flow rate. The performance of the proposed model is assessed using FID and compared with that of the LDM. The results are promising.

2 Generative displacement model (GDM)

Latent space is used to reduce computational cost, assuming that data in the latent space represent multiphase transport properties in porous media. Thus, the governing equations, which are empirical due to the complex pore structure, are implemented to simulate how one fluid displaces another that fully saturates the void space. The two fluids are immiscible, and the displacement occurs under pseudo-steady-state conditions. The displacing fluid is a wetting phase, while the other is non-wetting; this natural process is called imbibition. Once trained, the model can generate new samples; thus, it is referred to as the Generative Displacement Model (GDM).

Transport properties depend not only on the complex pore structure interacting with the fluid, but also on the occupying fluids. For instance, gas flows more easily than liquid. Thus, this study accounts for the occupied pore volumes as follows (Walsh and Lake 2003):

$$S_1 = \frac{V_1}{V_{\text{pore}}} \tag{1a}$$

$$S_2 = \frac{V_2}{V_{\text{pore}}} \tag{1b}$$

where S_1 is the saturation of the first fluid, V_1 is the volume of the first fluid in the pore space, V_{pore} is the pore volume, S_2 is the saturation of the second fluid, and V_2 is the volume of the second fluid in the pore space. The second saturation is the displacement saturation (S_D); thus, Eqs. (1a) and (1b) simplify as follows:

$$S_1 = 1 - S_2 = 1 - S_D \tag{2a}$$

$$S_D = S_2 \tag{2b}$$

Two transport properties are considered to implement the governing equations. First is the effective density, for which a volumetric average is used (Bird et al. 2002):

$$\rho_e = \sum_i \rho_i S_i = \rho_1 S_1 + \rho_2 S_2 = \rho_1(1 - S_D) + \rho_2 S_D \tag{3}$$

where ρ_e is the effective density, ρ_1 is the density of the first fluid, and ρ_2 is the density of the second fluid. Next, the study considers the total flow rate, expressed as follows (Lake et al. 2014):

$$q_1 = -\frac{k k_{r_1}}{\mu_1} A \nabla p_1 \tag{4a}$$

$$q_2 = -\frac{k k_{r_2}}{\mu_2} A \nabla p_2 \tag{4b}$$

where q_1 is the flow rate of the first fluid, k is the absolute permeability of the porous medium, k_{r_1} is the relative permeability of the first fluid, μ_1 is the viscosity of the first fluid, A is the cross-sectional area normal to the flow, and ∇p_1 is the pressure gradient applied to the first fluid. The flow rate of the second fluid is denoted by q_2, with relative permeability k_{r_2}, viscosity μ_2, and pressure gradient ∇p_2.

Absolute permeability indicates the ability of a porous medium to transmit a single-phase fluid. Higher permeability means a higher flow rate for a given pressure gradient. This ability decreases when two immiscible fluids occupy the void space; thus, relative permeability is introduced as a correction factor, as follows (Peters 2012):

$$k_{r_1} = k_{r_1}(S_D) \tag{5a}$$
$$k_{r_2} = k_{r_2}(S_D) \tag{5b}$$

Various models exist for relative permeability (Peters 2012; Bryant and Blunt 1992; Shanley et al. 2004). These relations are empirical because it is difficult to relate pore-scale processes (~10 nm–10 μm) to transport properties at a larger scale (~few centimeters). Relative permeability can be expressed using a power law with exponent n, or the Corey model (Peters 2012):

$$k_{r_1} = (1 - S_D)^n \quad \text{(Power law)} \tag{6a}$$
$$k_{r_2} = (S_D)^n \quad \text{(Power law)} \tag{6b}$$
$$k_{r_1} = (1 - S_D^2)(1 - S_D)^2 \quad \text{(Corey)} \tag{6c}$$
$$k_{r_2} = (S_D)^4 \quad \text{(Corey)} \tag{6d}$$

The difference between the pressures of the two fluids in Eqs. (4a) and (4b), referred to as capillary pressure, is negligible when the pore size is large, based on the Young–Laplace equation (Walsh and Lake 2003). Thus, the total flow rate is expressed by setting the pressure gradients equal ($\nabla p = \nabla p_1 = \nabla p_2$):

$$\frac{q_{\text{total}}}{-kA\nabla p} = \frac{1}{\mu_1} k_{r_1}(S_D) + \frac{1}{\mu_2} k_{r_2}(S_D) \tag{7}$$

The governing equations (3) and (7) allow an effective transport property to be obtained as follows:

$$z_e = z_1 w_1(S_D) + z_2 w_2(S_D) \tag{8}$$

where z_e is the effective transport property, z_1 is the transport property of the first fluid, $w_1(S_D)$ is the weight function of the first fluid, z_2 is the transport property of the second fluid, and $w_2(S_D)$ is the weight function of the second fluid. Table 1 summarizes the pertinent parameters.

Table 1: Parameters of the Generative Displacement Model (GDM).

Model	Fluid property ($i = 1, 2$)	$w_1(S_D)$	$w_2(S_D)$	Other parameters
Density	$z_i = \rho_i$	$1 - S_D$	S_D	None
Power-law (flow rate)	$z_i = \frac{1}{\mu_i}$	$(1 - S_D)^n$	S_D^n	n = 1.5, 2.0, 2.5, 3.0
Corey (flow rate)	$z_i = \frac{1}{\mu_i}$	$(1 - S_D^2)(1 - S_D)^2$	S_D^4	None

Next, this study analyzes the weight functions, whose variations with displacement saturation are shown in Figure 1. The density model provides the simplest trend, where both coefficients change linearly with displacement saturation (Figure 1a). The sum of its weight functions never exceeds unity because the effective property does not surpass that of either fluid (Figures 1a–f). While exceeding unity may not seem significant, it violates the fundamentals of multiphase transport. For density, a sum greater than unity would imply that a mixture of two fluids is denser than each fluid. A value greater than unity is also problematic for two-phase flow because it would imply that a fluid mixture flows faster than either fluid would alone.

3 Modifications to diffusion-based models

To shed further light on the weight functions, we discuss the mixing rule of diffusion-based models. Sohl-Dickstein et al. (2015) proposed the diffusion model based on non-equilibrium statistical physics, whose forward process generates samples as follows (Ho et al. 2020):

$$x_t = c_1(t)x_0 + c_2(t)\varepsilon \tag{9}$$

where x_t denotes the sample at time step t, $c_1(t)$ is the coefficient that indicates the fraction of the original sample x_0 that is preserved, and $c_2(t)$ controls the contribution of the Gaussian noise ε.

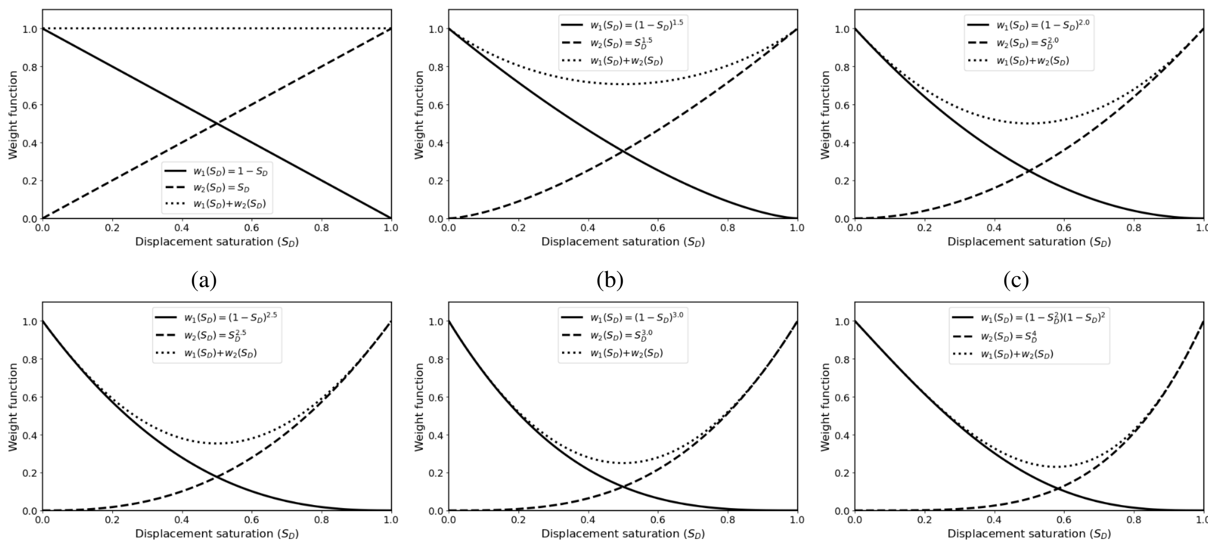

(a) (b) (c)

(d) (e) (f)

Figure 1: Weight functions of the Generative Displacement Model (GDM) summarized in Table 1.

Researchers have modified the noise schedule, sampling procedure, or parameterization, but the diffusion-based mixing rule itself has remained largely unchanged. For instance, Song et al. (2020) showed that images can be generated using a deterministic approach to speed up inference. Also, Nichol and Dhariwal (2021) observed empirically that performance improved when they adopted a cosine-squared schedule instead of a linear schedule. Additionally, Salimans and Ho (2022) proposed an alternative parameterization that predicts velocity rather than noise, which enhanced stability and sample quality.

Few studies have modified the mixing-rule coefficients. Table 2 lists the original coefficients and two modifications of diffusion-based models. Model 1 shows the original coefficients based on non-equilibrium statistical physics, calculated using a scaled-linear schedule. Later, Song et al. (2020) reported that exponential functions perform better. This empirical improvement is listed as the second model. Subsequently, Karras et al. (2022) modified the coefficients by analyzing the noise-to-signal ratio.

Table 2: Mixing-rule coefficients for the original diffusion model (Model 1) and two modifications (Models 2 and 3).

Model	Coefficients	Other parameters
1. Sohl-Dickstein et al. (2015)	First: $\sqrt{\bar{\alpha}_t}$ Second: $\sqrt{1-\bar{\alpha}_t}$	$\bar{\alpha}_t = \prod_{i=0}^{t}(1-\beta_i)$ β_i (Eq. 10) Diffusion time t
2. Song et al. (2020)	First: $f(\tau) = \exp\left[-0.25(\beta_{\max}-\beta_{\min})\tau^2 - 0.5\beta_{\min}\tau\right]$ Second: $g(\tau) = \sqrt{1-\exp[-0.5(\beta_{\max}-\beta_{\min})\tau^2 - \beta_{\min}\tau]}$	$\beta_{\min} = 0.1$ $\beta_{\max} = 20.0$ Dimensionless time $\tau = t/T$
3. Karras et al. (2022)	First (normalized): $\dfrac{1}{\sqrt{1+\sigma^2}}$ Second (normalized): $\dfrac{\sigma}{\sqrt{1+\sigma^2}}$	$\sigma(\tau) = \sigma_{\max}^{1-\tau}\sigma_{\min}^{\tau}$ $\sigma_{\min} = 0.002$; $\sigma_{\max} = 80.0$ $\tau = t/T$

Figure 2 demonstrates the variations of the coefficients versus normalized time. It also plots their summations, which are of interest in this study. Comparing Figures 2b and 2c with Figure 2a shows that the summations decrease from the original version and move closer to unity, improving performance. Reducing the overshoot is consistent with the GDM, where the sum of the weight functions does not exceed unity.

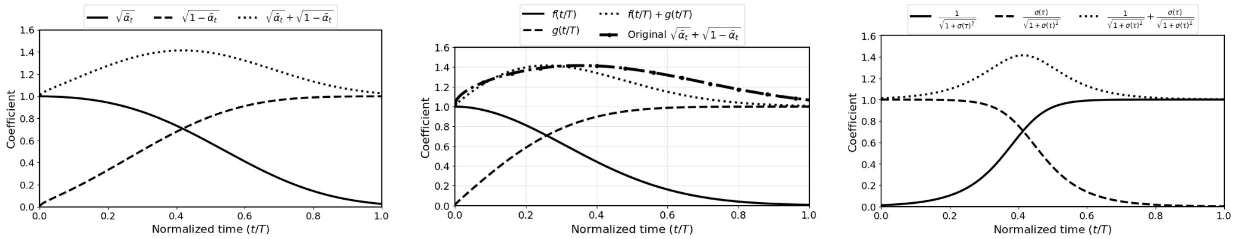

(a) (b) (c)

Figure 2: Variations of the coefficients versus normalized time for (a) Model 1, (b) Model 2, and (c) Model 3 listed in Table 2.

4 Shale fracture dataset

The proposed model is evaluated using complex fracture images of shale obtained from nanoindentations, a technique where an indenter tip penetrates a solid medium (Tabor 1948; Oliver and Pharr 1992). Recent studies show that fracture patterns encode quantitative information that can be used to train deep learning models to determine elastic modulus, hardness, and fracture toughness (Esatyana and Sakhaee-Pour 2025; Sakhaee-Pour 2025a, 2025b).

The central regions of 5,508 raw nanoindentation images of shale were cropped to 256×256 pixels for two reasons. This cropping focuses on complex fractures near the impression, rather than the surrounding region. Also, 256×256 pixels are commonly used in public AI datasets, for which numerous deep neural networks have been developed. Figure 3 shows examples of the cropped images under different loads, where each image size has 256×256 pixels (pixel size = 0.41 μm $\times$ 0.41 μm).

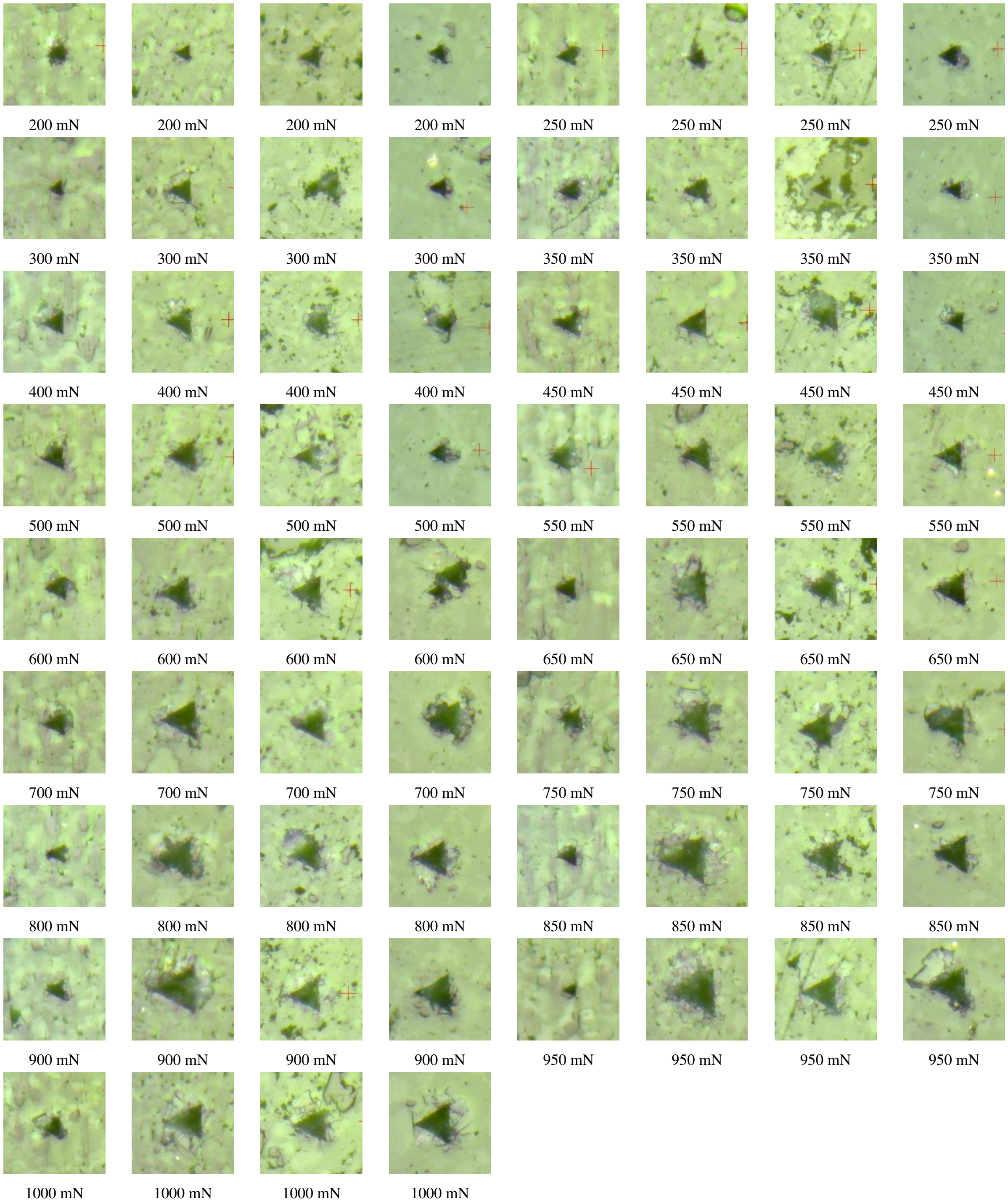

Figure 3: Examples of original shale images under various loads, where each image has 256×256 pixels (pixel size = 0.41 μm $\times$ 0.41 μm).

5 Results

The pixels were standardized, and the images were downsampled by a factor of 4 using a pretrained Vector Quantized Variational Autoencoder (Rombach et al. 2022) as a fixed encoder–decoder to obtain the latent space. Downsampling decreased the image size from $256 \times 256 \times 3$ to $64 \times 64 \times 3$. Then, a UNet was used to train the model. Figure 4 shows the architecture.

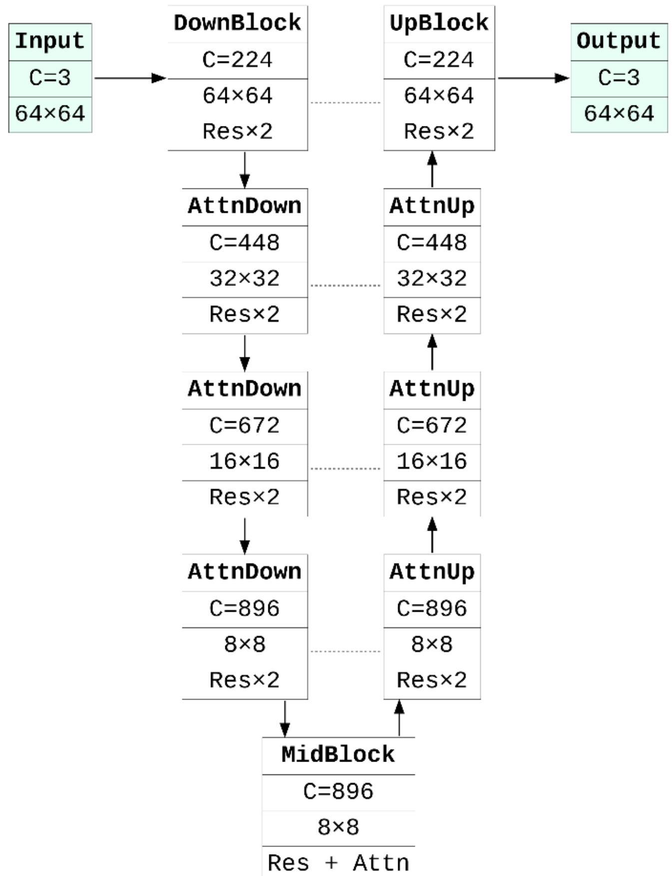

Figure 4: Architecture of the UNet used in this study (C = channels, Res = residual block, AttnDown = downsampling block + self-attention, AttnUp = upsampling block + self-attention).

This study applied 1,000 timesteps in the forward process to optimize the UNet parameters over 200,000 gradient update steps. Images were then generated from Gaussian noise over 200 inference steps. The forward process is a Markov chain, while image generation is deterministic, with no noise added between steps. This study used the scaled-linear schedule to train the LDM as follows:

$$\beta_t = \left(\sqrt{\beta_{\text{start}}} + \frac{t}{999}\left(\sqrt{\beta_{\text{end}}} - \sqrt{\beta_{\text{start}}}\right)\right)^2, \qquad t = 0 \text{ to } 999 \tag{10}$$

where β_t is the noise schedule, and β_{start} and β_{end} are the schedule endpoints set to 0.0001 and 0.02, respectively. This study also used the same coefficients for the displacement saturation ($S_D = \bar{\alpha}_t$) for comparison. It then implemented the weight functions listed in Table 1.

The transport property of the displacing fluid was set to Gaussian noise with unit standard deviation and zero mean. Errors were then predicted. The weights were subsequently updated by minimizing the difference between the actual error (e) and the predicted error (e_θ) as follows:

$$L = \mathbb{E}_{t,x_0,e}\left[\|e - e_\theta(x_t, t)\|^2\right] \tag{11}$$

The UNet weights were initialized based on values reported for human faces after training for 2M steps using LDM (Rombach et al. 2022). The public human-face dataset, referred to as CelebA-HQ, includes 256×256 color images. An exponential moving average was also used during training with a decay of 0.9999. The Adam optimizer was applied, and a grid search over learning rates (LRs) was conducted to identify optimal settings. The learning rates were 1×10^{-5}, 2×10^{-5}, 3×10^{-5}, 4×10^{-5}, and 5×10^{-5}. Training each model for 200k gradient update steps and assessing its performance lasted approximately 21 hours on an A100 GPU.

This study used FID to assess performance. The FID was calculated every 5k gradient update steps using 1,000 generated images, compared with 5,508 original images of complex fractures. Figure 5 shows the results. The FID of the density model decreases faster with epoch than that of the other models because it is the simplest and perhaps more intuitive for the UNet. This is followed by the LDM, where the sum of its coefficients overshoots unity. Next are the power-law and Corey models.

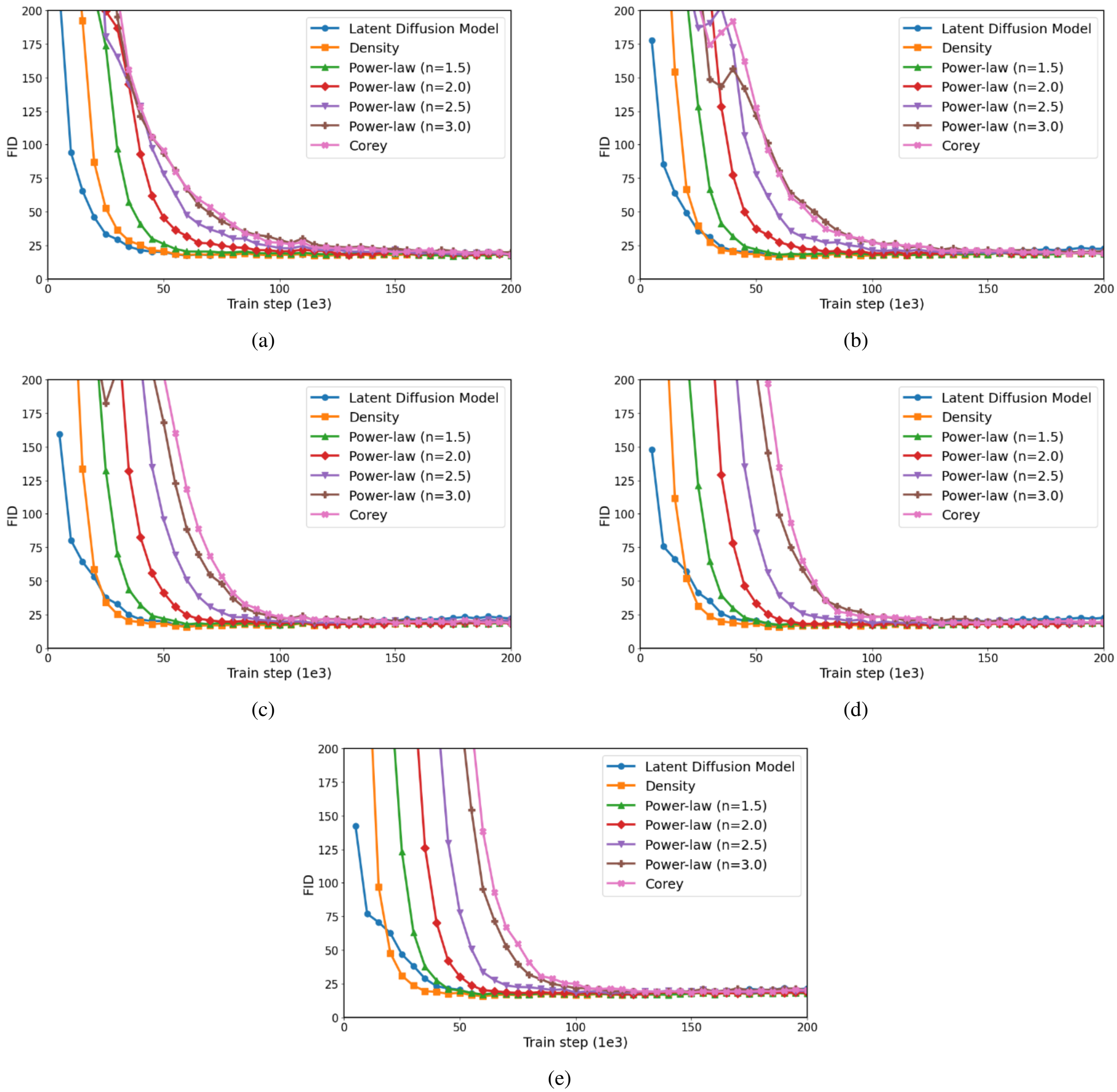

Figure 5: Variations of FID over 200k steps for (a) LR=1×10^{-5}, (b) LR=2×10^{-5}, (c) LR=3×10^{-5}, (d) LR=4×10^{-5}, and (e) LR=5×10^{-5}.

This study conducted a grid search over learning rates without fine-tuning other hyperparameters, and the results are relatively similar. The slightly better performance of the LDM compared to the power-law and Corey models may be due to using the scaled-linear schedule originally designed for LDM. Another contributing factor may be initializing weights based on values reported after 2M training steps of LDM. This non-random initialization decreases computational cost.

Table 3 summarizes the best FID values. The GDM with density achieved the lowest FID, reaching 15.7 at 60k training steps with a learning rate of 4×10^{-5}, comparable to the LDM's best FID of 16.6 under the same conditions. Next was the GDM with the power-law model ($n = 1.5$), achieving an FID of 16.7 at 140k training steps with a learning rate of 5×10^{-5}. In general, GDM performed better when the sum of the weight functions was closer to unity and deteriorated as the power-law exponent increased. The improved performance of GDM with a closer-to-unity summation is consistent with the improvements in the LDM discussed earlier.

There is no significant difference among the results in Table 3. The Corey model reached its best FID later because the original image provided little meaningful information during the last quarter of training. Its second weight function is less than or equal to 0.027, with a signal-to-noise ratio of eight percent or less when displacement saturation is greater than or equal to 0.75, leading to Gaussian noise dominating the data. This lack of useful information over a wide range of training also applies to the power-law model with an exponent of 3.

Table 3: Best FID values of the Latent Diffusion Model (LDM) and Generative Displacement Model (GDM) for different learning rates (LRs) over 200k training steps.

Model	Governing relation	LR=1e-5	LR=2e-5	LR=3e-5	LR=4e-5	LR=5e-5
LDM	Diffusion	17.4 @ 60k	17.1 @ 60k	16.8 @ 60k	16.6 @ 60k	17.0 @ 60k
GDM	Density	17.2 @ 115k	16.4 @ 60k	15.9 @ 60k	15.7 @ 60k	15.7 @ 60k
GDM	Power-law (n=1.5)	17.0 @ 175k	17.7 @ 115k	17.3 @ 100k	17.2 @ 100k	16.7 @ 140k
GDM	Power-law (n=2.0)	17.8 @ 185k	18.3 @ 115k	17.5 @ 120k	17.2 @ 100k	17.1 @ 125k
GDM	Power-law (n=2.5)	18.2 @ 200k	18.4 @ 175k	18.7 @ 115k	18.2 @ 130k	17.9 @ 115k
GDM	Power-law (n=3.0)	19.3 @ 180k	19.1 @ 175k	18.8 @ 175k	19.2 @ 165k	18.7 @ 130k
GDM	Corey	17.9 @ 200k	18.6 @ 185k	18.5 @ 150k	18.5 @ 130k	18.3 @ 150k

Next, this study generated complex fractures using the trained models with the best FID values. Figure 6 shows the generated images, which are realistic compared with the original images shown in Figure 3. The generated images exhibit impressions of different sizes, and the fracture patterns are distinct. Moreover, the rock surface patterns far from the impression are varied and realistic.

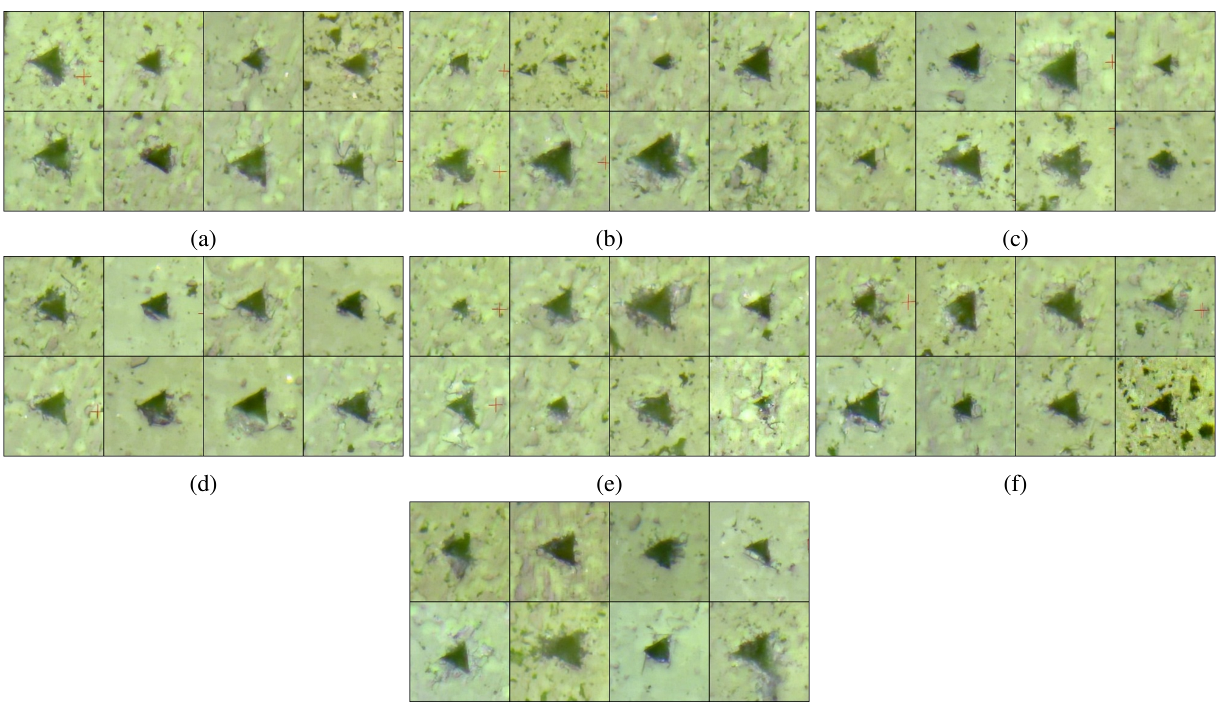

(a) (b) (c) (d) (e) (f) (g)

Figure 6: Generated images (256×256 pixels; each pixel is 0.41 μm $\times$ 0.41 μm) using (a) the Latent Diffusion Model (FID = 16.6) and the Generative Displacement Models with (b) density (FID = 15.7), (c) power-law model ($n = 1.5$, FID = 16.7), (d) power-law model ($n = 2.0$, FID = 17.1), (e) power-law model ($n = 2.5$, FID = 17.9), (f) power-law model ($n = 3.0$, FID = 18.7), and (g) Corey model (FID = 17.9).

6 Discussion

The best FID in this study is higher than the values reported for larger datasets. For instance, the LDM achieved an FID of 5.11 when generating human faces using the CelebA-HQ dataset (Rombach et al. 2022). This difference arises because this study used 5,508 color images, while the CelebA-HQ dataset contains 30,000 images. Fewer images negatively impact performance. The dataset in this study is smaller because subsurface samples are more challenging to obtain and test using indentation. The lack of large datasets, in fact, provides an incentive for developing generative models.

The objective of this study was not to achieve the lowest possible FID for complex fractures. The main objective was to propose a new generative model based on multiphase transport in porous media, whose performance remains comparable to that of the LDM. GDM performance may improve with further hyperparameter tuning. Nevertheless, the GDM results, especially for the density-based model, are promising. Other transport properties not explored in this study may also yield good results.

This study trained a deep neural network to simulate how one fluid displaces another. The property of the displacing fluid was set to Gaussian noise, while the first fluid was based on a complex fracture. Once the model was trained, a reverse process generated images from Gaussian noise. Other random distributions may also yield realistic results.

7 Conclusions

This study introduced a Generative Displacement Model (GDM) inspired by multiphase transport in porous media. Unlike existing generative models derived from molecular diffusion or game theory, the GDM incorporates transport-based weight functions into the latent space. The GDM was evaluated using 5,508 fracture images of shale and compared with a Latent Diffusion Model (LDM). The GDM yielded its lowest FID using the density model, reaching 15.7 at 60k training steps with a learning rate of 4×10^{-5}, comparable to the LDM's best FID of 16.6 under the same conditions; the power-law model followed closely with an FID of 16.7. The grid search targeted learning rates; therefore, the comparison may underestimate the full potential of GDM. Model performance tracked how closely the weight functions summed to unity, consistent with the constraint that an effective property cannot exceed that of either constituent fluid. The trained models generated realistic complex fractures. These results suggest that transport processes in porous media are promising for future generative model design.

8 Declarations

The author used LLMs to improve the language, readability, and formatting of the manuscript. The author reviewed and edited the content as needed and takes full responsibility for the content.

References

[1] Alipour, M., Esatyana, E., Sakhaee-Pour, A., Sadooni, F.N., Al-Kuwari, H.A., 2021. Characterizing fracture toughness using machine learning. Journal of Petroleum Science and Engineering 200, 108202. https://doi.org/10.1016/j.petrol.2020.108202

[2] Amiri, H., Vasconcelos, I., Jiao, Y., Chen, P.E., Plümper, O., 2023. Quantifying microstructures of earth materials using higher-order spatial correlations and deep generative adversarial networks. Scientific Reports 13, 1805. https://doi.org/10.1038/s41598-023-28970-w

[3] Benson, S.M., Cole, D.R., 2008. CO_2 sequestration in deep sedimentary formations. Elements 4, 325–331. https://doi.org/10.2113/gselements.4.5.325

[4] Bird, R.B., Stewart, W.E., Lightfoot, E.N., 2002. Transport Phenomena, 2nd ed. Wiley, New York.

[5] Bryant, S., Blunt, M., 1992. Prediction of relative permeability in simple porous media. Phys. Rev. A 46, 2004. https://doi.org/10.1103/PhysRevA.46.2004

[6] Chollet, F., 2021. Deep Learning with Python, 2nd ed. Simon & Schuster, New York, NY.

[7] de Castro Vargas Fernandes, J., Duarte Vidal, A., Carvalho Medeiros, L., Menezes dos Anjos, C.E., Surmas, R., Gonçalves Evsukoff, A., 2024. Absolute permeability estimation from microtomography rock images through deep learning super-resolution and adversarial fine tuning. Scientific Reports 14, 16704. https://doi.org/10.1038/s41598-024-67367-1

[8] Esatyana, E., Sakhaee-Pour, A., 2025. Deep learning for upscaling nanoindentation images. Theoretical and Applied Fracture Mechanics 139, 105065. https://doi.org/10.1016/j.tafmec.2025.105065

[9] Fan, W., Liu, G., Chen, Q., Cui, Z., Wu, X., Zhang, Z., 2024. Stochastic reconstruction of geological reservoir models based on a concurrent multi-stage U-Net generative adversarial network. Computers and Geosciences 186, 105562. https://doi.org/10.1016/j.cageo.2024.105562

[10] Ferreira, I., Ochoa, L., Koeshidayatullah, A., 2022. On the generation of realistic synthetic petrographic datasets using a style-based GAN. Scientific Reports 12, 12845. https://doi.org/10.1038/s41598-022-16034-4

[11] Goodfellow, I., Bengio, Y., Courville, A., 2016. Deep Learning. MIT Press, Cambridge, MA.

[12] Goodfellow, I., Pouget-Abadie, J., Mirza, M., Xu, B., Warde-Farley, D., Ozair, S., Bengio, Y., 2014. Generative adversarial nets. Advances in Neural Information Processing Systems 27, 2672–2680.

[13] Ho, J., Jain, A., Abbeel, P., 2020. Denoising diffusion probabilistic models. Advances in Neural Information Processing Systems 33, 6840–6851.

[14] Karras, T., Aittala, M., Aila, T., Laine, S., 2022. Elucidating the design space of diffusion-based generative models. Advances in Neural Information Processing Systems 35, 26565–26577.

[15] Lake, L.W., Johns, R.T., Rossen, W.R., Pope, G.A., 2014. Fundamentals of Enhanced Oil Recovery. Society of Petroleum Engineers, Richardson, TX.

[16] Lyu, X., Ren, X., 2024. Microstructure reconstruction of 2D/3D random materials via diffusion-based deep generative models. Scientific Reports 14, 5041. https://doi.org/10.1038/s41598-024-54861-9

[17] Nguyen, P.C.H., Vlassis, N.N., Bahmani, B., Sun, W., Udaykumar, H.S., Baek, S.S., 2022. Synthesizing controlled microstructures of porous media using generative adversarial networks and reinforcement learning. Scientific Reports 12, 9034. https://doi.org/10.1038/s41598-022-12845-7

[18] Nichol, A.Q., Dhariwal, P., 2021. Improved denoising diffusion probabilistic models. In: Proceedings of the 38th International Conference on Machine Learning, pp. 8162–8171.

[19] Oliver, W.C., Pharr, G.M., 1992. An improved technique for determining hardness and elastic modulus. Journal of Materials Research 7, 1564–1583. https://doi.org/10.1557/JMR.1992.1564

[20] Peters, E.J., 2012. Advanced Petrophysics, Vol. 2. Greenleaf Book Group, Austin, TX.

[21] Ranazzi, P.H., Luo, X., Sampaio, M.A., 2024. Improving the training performance of generative adversarial networks with limited data: Application to the generation of geological models. Computers and Geosciences 193, 105747. https://doi.org/10.1016/j.cageo.2024.105747

[22] Rombach, R., Blattmann, A., Lorenz, D., Esser, P., Ommer, B., 2022. High-resolution image synthesis with latent diffusion models. In: Proceedings of the IEEE/CVF Conference on Computer Vision and Pattern Recognition, pp. 10684–10695.

[23] Sahimi, A., Sahimi, M., 2025. Machine learning and digital images of porous materials: from rock to the human brain. Frontiers in Physics 13, 1742403. https://doi.org/10.3389/fphy.2025.1742403

[24] Sahimi, M., 2025. Artificial Intelligence in Science and Engineering: From Porous Materials to Drug Discovery. Wiley-VCH, Weinheim.

[25] Sakhaee-Pour, A., Bryant, S.L., 2012. Gas permeability of shale. SPE Reservoir Evaluation and Engineering 15, 401–409. https://doi.org/10.2118/146944-PA

[26] Sakhaee-Pour, A., 2025a. Deep learning for characterizing fracture toughness. Theoretical and Applied Fracture Mechanics 135, 104759. https://doi.org/10.1016/j.tafmec.2024.104759

[27] Sakhaee-Pour, A., 2025b. Deep learning for interpreting elastic modulus and hardness. Engineering Fracture Mechanics 320, 111074. https://doi.org/10.1016/j.engfracmech.2025.111074

[28] Salimans, T., Ho, J., 2022. Progressive distillation for fast sampling of diffusion models. arXiv preprint arXiv:2202.00512. https://doi.org/10.48550/arXiv.2202.00512

[29] Salimzadeh, S., Kasperczyk, D., Kadeethum, T., 2023. A surrogate model for predicting ground surface deformation gradient induced by pressurized fractures. Advances in Water Resources 181, 104556. https://doi.org/10.1016/j.advwatres.2023.104556

[30] Shanley, K.W., Cluff, R.M., Robinson, J.W., 2004. Factors controlling prolific gas production from low-permeability sandstone reservoirs. AAPG Bulletin 88, 1083–1121. https://doi.org/10.1306/03250403051

[31] Sohl-Dickstein, J., Weiss, E., Maheswaranathan, N., Ganguli, S., 2015. Deep unsupervised learning using nonequilibrium thermodynamics. In: Proceedings of the 32nd International Conference on Machine Learning, pp. 2256–2265.

[32] Song, Y., Sohl-Dickstein, J., Kingma, D.P., Kumar, A., Ermon, S., Poole, B., 2020. Score-based generative modeling through stochastic differential equations. arXiv preprint arXiv:2011.13456. https://doi.org/10.48550/arXiv.2011.13456

[33] Tabor, D., 1948. A simple theory of static and dynamic hardness. Proceedings of the Royal Society A 192, 247–274. https://doi.org/10.1098/rspa.1948.0008

[34] Ugolkov, E., He, X., Kwak, H., Hoteit, H., 2025. Optimized generative adversarial network for efficient resolution enhancement of 3D segmented rock tomography. Scientific Reports 15, 37492. https://doi.org/10.1038/s41598-025-21624-z

[35] Walsh, M., Lake, L.W., 2003. A generalized approach to primary hydrocarbon recovery. Society of Petroleum Engineers.

[36] Zhang, T., Hu, G., Yang, Y., Du, Y., 2023. A super-resolution reconstruction method for shale based on generative adversarial network. Transport in Porous Media 150, 383–426. https://doi.org/10.1007/s11242-023-02016-1

[37] Zhu, L., Bijeljic, B., Blunt, M.J., 2024. Generation of pore-space images using improved pyramid Wasserstein generative adversarial networks. Advances in Water Resources 190, 104748. https://doi.org/10.1016/j.advwatres.2024.104748

[38] Zivar, D., Kumar, S., Foroozesh, J., 2021. Underground hydrogen storage: A comprehensive review. International Journal of Hydrogen Energy 46, 23436–23462. https://doi.org/10.1016/j.ijhydene.2020.08.138